High-Resolution Simulation of Shallow-to-Deep Convection Transition over Land

Marat Khairoutdinov and David Randall

Department of Atmospheric Science, Colorado State University, Fort Collins, Colorado

ABSTRACT

Results are presented from a high-resolution three-dimensional simulation of shallow-to-deep convection transition based on idealization of observations made during the Large-Scale Biosphere–Atmosphere (LBA) experiment in Amazonia, Brazil, during the Tropical Rainfall Measuring Mission (TRMM)-LBA mission on 23 February. The doubly periodic grid has $1536 \times 1536 \times 256$ grid cells with horizontal grid spacing of 100 m, thus covering an area of 154×154 km^2. The vertical resolution varies from 50 m in the boundary layer to 100 m in the free troposphere and gradually coarsens to 250 m near the domain top at 25.4 km. The length of the simulation is 6 h, starting from an early morning sounding corresponding to 0730 local time. Convection is forced by prescribed surface latent and sensible heat fluxes and prescribed horizontally uniform radiative heating

Despite a considerable amount of convective available potential energy (CAPE) in the range of 1600–2400 J kg^{-1}, and despite virtually no convective inhibition (CIN) in the mean sounding throughout the simulation, the cumulus convection starts as shallow, gradually developing into congestus, and becomes deep only toward the end of simulation. Analysis shows that the reason is that the shallow clouds generated by the boundary layer turbulence are too small to penetrate deep into the troposphere, as they are quickly diluted by mixing with the environment. Precipitation and the associated cold pools are needed to generate thermals big enough to support the growth of deep clouds. This positive feedback involving precipitation is supported by a sensitivity experiment in which the cold pools are effectively eliminated by artificially switching off the evaporation of precipitation; in the experiment, the convection remains shallow throughout the entire simulation, with a few congestus but no deep clouds.

The probability distribution function (PDF) of cloud size during the shallow, congestus, and deep phases is analyzed using a new method. During each of the three phases, the shallow clouds dominate the mode of the PDFs at about 1-km diameter. During the deep phase, the PDFs show cloud bases as wide as 4 km. Analysis of the joint PDFs of cloud size and in-cloud variables demonstrates that, as expected, the bigger clouds are far less diluted above their bases than their smaller counterparts. Also, thermodynamic properties at cloud bases are found to be nearly identical for all cloud sizes, with the moist static energy exceeding the mean value by as much as 4 kJ kg^{-1}. The width of the moist static energy distribution in the boundary layer is mostly due to variability of water vapor; therefore, clouds appear to grow from the air with the highest water vapor content available.

No undiluted cloudy parcels are found near the level of neutral buoyancy. It appears that a simple entraining-plume model explains the entrainment rates rather well. The least diluted plumes in the simulation correspond to an entrainment parameter of about 0.1 km^{-1}.

1. Introduction

Despite substantial progress made over the past decades, the representation of convection in large-scale models remains a difficult problem (e.g., Randall et al. 2003a; Arakawa 2004). It is well known that general circulation models (GCMs) with parameterized convection have considerable difficulty in representing the diurnal cycle of convection and precipitation over the summertime continents (e.g., Betts and Jakob 2002; Bechtold et al. 2004). The problem manifests itself most noticeably as a tendency for precipitation to reach its maximum several hours too early, compared to observations.

One of the reasons for this bias may be the fact that convective parameterizations in GCMs generally use the large-scale (which is the same as the grid scale in

Corresponding author address: Marat Khairoutdinov, Department of Atmospheric Science, Colorado State University, Fort Collins, CO 80523.
E-mail: marat@atmos.colostate.edu

most GCMs) characteristics such as convective available potential energy (CAPE), among others, to predict the timing and strength of convection. The diurnal cycle, on the other hand, is a more localized response of rapidly developing convection to solar heating of the surface in the form of circulations, unresolved by GCMs (subgrid-scale), associated with nonuniform heating in the presence of terrain (e.g., Redelsperger and Clark 1990) and other land surface heterogeneity (e.g., Avissar 1995), sea breeze (e.g., Wakimoto and Atkins 1994), cold pools, and gust fronts due to evaporating precipitation (e.g., Wakimoto 1982; Kingsmill 1995), drylines (e.g., Bluestein and Parker 1993), horizontal convective rolls (e.g., Weckwerth et al. 1996), etc.

The relatively new "superparameterization" approach to general circulation modeling (Grabowski 2001; Khairoutdinov and Randall 2001; Khairoutdinov et al. 2005) has the advantage of explicitly including the sub-GCM/grid-scale dynamics by replacing the cloud parameterization with a cloud-resolving model inserted into each GCM grid. It has been demonstrated (Khairoutdinov et al. 2005) that such a modified GCM appears to considerably improve the simulated diurnal cycle of precipitation over summertime continents when compared to the standard version of the same GCM. Such an approach, however, comes with very high computational cost and has not yet been used for prolonged climate-change simulations. In any case, the representation of the diurnal cycle in conventional GCMs still needs to be improved.

Over the past two decades or so, major progress in our understanding of convection has been driven through the widespread use of cloud-resolving models (CRMs). They have extensively been used to evaluate and improve existing parameterizations, as well as to inspire new approaches. Without doubt, CRMs have their own share of problems and issues. Among them are the effects of domain geometry, size, and grid resolution, the numerical algorithms used, subgrid-scale turbulence parameterizations, highly parameterized and uncertain microphysics parameterizations, etc. Some of the problems associated with the grid resolution and domain geometry will be mitigated over time as more powerful supercomputers become available. Other issues such as the realism of cloud microphysics parameterizations will be much more persistent. Despite these problems, CRMs can be placed at the top of the cloud model hierarchy, largely based on the results of many case studies that have demonstrated that CRMs generally produce more realistic results than models that use parameterizations (e.g., Randall et al. 2003b).

This study has grown from our participation in the CRM intercomparison activities within the Working Group 4 (Precipitating Convective Cloud Systems) of the Global Energy and Water Cycle Experiment (GEWEX) Cloud System Study (GCSS). The simulated case was based on idealization of observations made during the Large-Scale Biosphere–Atmosphere (LBA) experiment in Amazonia, Brazil, in the boreal winter of 1999 (Silva Dias et al. 2002). The main focus of the case study was on the transition from the early morning shallow cumuli to afternoon deep convection, which is a typical diurnal evolution in the Amazon in boreal winter. More details on the case are given in the next section.

In this study, we describe the results of three-dimensional simulation of the shallow-to-deep cumulus transition over an area 150 km across, with a horizontal resolution of 100 m and vertical resolution as high as 50 m in the boundary layer and 100 m elsewhere in the troposphere. Similar resolution was used in a study of shallow-to-deep cumulus transition over the ocean recently reported by Kuang and Bretherton (2005, hereafter referred to as KB05); however, they used a much smaller domain size of about 20 km.

Note that, even though the boundary layer turbulence and shallow convection were only marginally resolved in this study, the grid spacing was close to that typically used by LES models of shallow convection (e.g., Siebesma et al. 2003) and about one order of magnitude finer than the typical resolution used in CRM simulations of deep convection. An order-of-magnitude decrease of the grid spacing, keeping the domain size the same, implies at least a 10 000-fold increase in the required computational resources, which explains why so few high-resolution studies of deep convection have been conducted so far.

The model and simulation setup are described in section 2. Section 3 describes the main results of the high-resolution run. Section 4 presents several results of sensitivity study with a lower-resolution model. The main findings are summarized in section 5.

2. Model description and simulation setup

The cloud-resolving model used in this study is the System for Atmospheric Modeling (SAM; Khairoutdinov and Randall 2003). SAM solves the equations of motion using the anelastic approximation. The thermodynamics are described by three prognostic variables: the total nonprecipitating water composed of water vapor and cloud liquid/ice condensate, total precipitating water, and liquid/ice static energy, whose definition

uses both nonprecipitating and precipitating water, assuming exact conservation under moist adiabatic processes, except for gravitational sedimentation and fallout. Six different types of water substance, that is, vapor, cloud water, cloud ice, rain, snow, and graupel, are uniquely diagnosed from the prognostic thermodynamic variables, assuming that the partitioning between the liquid and ice phases depends on temperature only.

The conversion rates among the various water substances are parameterized using bulk microphysics rates describing such processes as autoconversion of cloud water to rain, aggregation of cloud ice to snow/graupel, accretional growth of hydrometeors by collecting nonprecipitating condensate, and gravitational sedimentation. The rates computed for each water species are used to compute the rates of change of prognostic thermodynamic variables. Because of the particular definition of the liquid/ice static energy, the freezing and melting processes are implicitly included. The use of only two prognostic water variables instead of six allows one to speed up the computations quite considerably.

The finite difference representation of the model equations uses the Arakawa C staggering, with stretched vertical and uniform horizontal grids. The advection and diffusion of momentum are second-order accurate, with kinetic energy conservation under advection. Time integration of momentum equations is done using the third-order Adams–Bashforth scheme with variable time stepping to maintain linear stability. In this particular study, the subgrid-scale (SGS) fluxes have been parameterized using a Smagorinsky-type closure; however, a so-called 1.5-order SGS closure based on prognostic SGS turbulent kinetic energy is also available. Advection of all scalar prognostic variables is done using a monotonic and positive-definite advection scheme in flux form. A Newtonian damping layer is implemented in the upper third of the domain to reduce gravity wave reflection and buildup.

The simulation design closely follows specification for Case 4 of the GCSS Working Group 4. The case is based on idealization of observations made during the LBA experiment in Amazonia during the Tropical Rainfall Measuring Mission (TRMM)-LBA ground validation program mission on 23 February 1999. Detailed case specifications along with the results from several participating models, including SAM, are described by Grabowski et al. (2006). Convection is forced for 6 hours by prescribed surface latent and sensible heat fluxes as well as by the prescribed radiative heating profile. The forcing is horizontally uniform at each level, across the domain. The simulation starts at 0730 local time (all times LT), when the prescribed surface latent and sensible heat fluxes are zero. The fluxes reach maxima of 554 and 270 W m^{-2}, respectively, about 5 h later, at 1245.

The doubly periodic grid had $1536 \times 1536 \times 256$ grid cells with a horizontal grid spacing of 100 m, thus covering an area of 154×154 km^2, which was sufficient to contain lots of individual clouds, allowing us to compute meaningful statistics for the short 6-h simulation. The vertical grid spacing was varying with height, from 50 m below 1.5 km, increasing to 100 m at 6 km, staying 100 m all the way up to 18 km, and gradually degrading to 250 m near the domain top at 25.4 km. The time step was 2 s. To initialize turbulence, a random small-amplitude noise was added to the temperature field near the surface. No noise was added at later times.

SAM uses the Message-Passing Interface (MPI) protocol to utilize parallel computers. Parallelization is based on horizontal domain decomposition. The high-resolution simulation was performed using 128 processors of the "Bluesky" IBM-SP supercomputer at the National Center for Atmospheric Research and took about two weeks of wall-clock time to complete.

3. Results

a. Time evolution

Figure 1 shows the evolution with time of the horizontally averaged nonprecipitating condensate, precipitating water, and precipitation rate. The prescribed surface fluxes are also shown. The first shallow clouds appear about 2 h into the simulation, that is, at 0930. As the surface fluxes increase, the clouds grow taller, and the amount of condensate increases correspondingly. Shortly after hour 3 (1030), the first light rain reaches the surface. As clouds grow past the freezing level at about 5 km, the ice microphysics is engaged, which leads to a rather dramatic spinup in the production of precipitation. After 5 h (1230), one hour before the end of the simulation, deep clouds emerge with tops as high as 12 km. The shallow and midlevel convection nevertheless continue to dominate the skies, with tops predominantly below 6 km. The simulated cloud field as would be seen from the surface at the simulation's end is illustrated in Fig. 2. One can see that with 100-m grid spacing, the simulated clouds do appear quite turbulent.

The evolution of the convective boundary layer (CBL) and the clouds during the shallow-cloud phase is further illustrated in Fig. 3, which shows the evolution of the mean cloud condensate amount and vertical velocity variance. One can see that the lifting condensa-
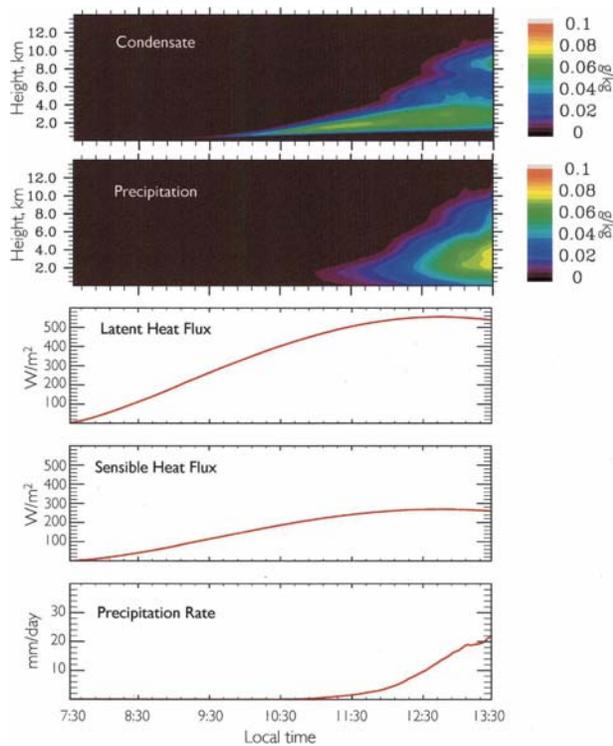
FIG. 1. Time evolution of mean profiles of nonprecipitating cloud condensate, precipitating water, as well as time series of the surface latent and sensible heat fluxes and precipitation rate.

tion level is always collocated with the CBL top, conventionally defined as the height where the buoyancy flux has a local minimum. Before 1030, the shallow clouds do not reach the level of free convection, as can be inferred from monotonic decreases of $\overline{w^2}$ above the CBL. Later, $\overline{w^2}$ acquires a maximum above the CBL, whose position is marked by the red solid line. This indicates that clouds penetrate above the level of free convection and accelerate upward, but apparently quickly loose buoyancy due to entrainment. As the surface fluxes continue to increase, the CBL eddies that give rise to clouds become more moist and buoyant and penetrate progressively deeper into the lower troposphere before being diluted by entrainment. The CBL and clouds continue to evolve quite monotonically until after five simulated hours, when the convective regime abruptly changes as deep convection develops.

Figure 4 compares soundings between the shallow convective regime at 1130 and the deep convective regime at 1330. Each sounding is also contrasted against the initial early morning sounding. The maximum cloud-top height for each sounding is indicated by a horizontal green line. One can notice that the early morning troposphere has a considerable amount of

convective available potential energy,[1] about 1600 J kg^{-1}. Convection is prevented by the stable boundary layer and a rather considerable amount of convective inhibition energy (CIN) of about 15 J kg^{-1}. By 1130, the sounding shows a well-mixed 1-km-deep CBL with a CAPE of 2200 J kg^{-1}, which is slightly larger than the CAPE of the early morning sounding. By 1130, the CIN of the mean sounding is virtually eliminated, and convection is quite active, with positively buoyant and accelerating clouds; yet, they do not develop or penetrate above 4 km. During the next two hours, an abrupt transition of convection from shallow to deep occurs with cloud tops reaching levels as high as 12 km, while the sounding has changed relatively little, with the CAPE increasing to 2400 J kg^{-1}.

What causes such a rapid reorganization and deepening of the simulated convection? Inspection of three-dimensional fields provides some insight. For example, Fig. 5 shows zoomed-in horizontal cross sections of the moist static energy[2] (MSE) field at a height of 500 m, or approximately in the middle of the CBL, over a 30×30 km^2 area, at 1130 and 1330. One can see that during the shallow convective regime (1130) the CBL contains eddies that are generally less than 1 km across. During the deep convective regime (1330), the eddies tend to coagulate into large coherent structures aligned along the gust fronts or density currents, which are the moving edges of the cold pools. These cold pools are created by downdrafts that contain the negatively buoyant air cooled by evaporation of rain above the CBL. This can be seen from much smaller values of the MSE in the middle of the cold pools in Fig. 5. Because MSE is conserved during evaporation of water, the air with low values of MSE must have been brought down from above the CBL, where the MSE profile has a minimum.

The importance of the cold pools can be seen in Fig. 6, which is similar to Fig. 5 but shows the horizontal cross sections at 3 km. The clouds are shown by masking the moist static energy field. One can see that not only do clouds tend to form above the cold pool edges, as noted by Tompkins (2001b), but also, as found by KB05, they tend to be bigger than the clouds that form

---

[1] CAPE is proportional to the area between the red curve representing the trajectory of an undiluted parcel, taken near the surface and lifted pseudoadiabatically from the level of free convection to the level of neutral buoyancy, and the temperature profile. CIN is a measure of energy it takes for a parcel to overcome a stable layer below the level of free convection.

[2] Moist static energy h is defined as $h = C_p T + gz + L q_v$, where T is air temperature; g acceleration due to gravity; C_p specific heat for air; L specific heat of condensation; z height; and q_v is water vapor mixing ratio.

FIG. 2. Visualization of the simulated cloud field at 0130 in the afternoon as would be seen from the surface. Note that the clouds on the left are as high as 12 km.

in the CBL without cold pools. As discussed further below, large clouds entrain relatively less than small clouds, which enables them to maintain less diluted cores and, hence, penetrate deeper into the troposphere. Thus, precipitation and the associated cold pool dynamics appear to be essential for the shallow-to-deep convection transition simulated in this study. This notion will be directly tested in one of the sensitivity experiments discussed in section 4.

b. Cloud size distribution

Notably, at 1330 LT only a few clouds in Fig. 6 are considerably larger than the clouds at earlier times; there are still plenty of small clouds as well. Therefore, a simple mean cloud size alone may not be sufficient to characterize the evolution of the cloud population; a cloud size probability distribution function (PDF) may be more useful. Sampling clouds by their size would enable us to conditionally sample in-cloud statistics to see how they change with cloud size. By cloud size we mean some measure of size of the horizontal footprint of a cloud.

The sampling algorithm used in this study is illustrated in Fig. 7. Starting from any cloudy pixel, we measure the distances a_i to the cloud edge along two perpendicular directions. As clouds can have irregular shapes, directional averaging is also done by making measurements along two more directions rotated by 45° with respect to the original directions; thus, a total of eight measurements are taken. The cloud size, D, measured from this particular cloudy pixel is then com-

puted as twice the square root of the mean-squared distance:

$$D = 2 \sqrt{\frac{1}{8} \sum_{i=1}^{i=8} a_i^2}. \tag{1}$$

It can be shown that, in the case of clouds with a circular shape, the computed cloud size will always be equal to the cloud diameter, regardless of the position of the starting point within that cloud. Therefore, for the hypothetical circular-cloud population of the same size, the algorithm would yield a monodisperse PDF. Note that this algorithm is only suited for cloud populations that consist mostly of clouds with more or less round and regular shapes, as in this study, and may
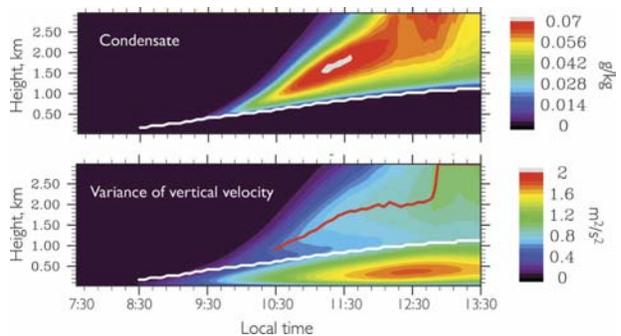

FIG. 3. Time evolution of the mean profiles of (top) nonprecipitating cloud condensate and (bottom) variance of the vertical velocity. The boundary layer top is defined as the height of the minimum of buoyancy flux, and is identified by the white line. The position of the secondary maximum of the vertical velocity variance is shown by the red line.
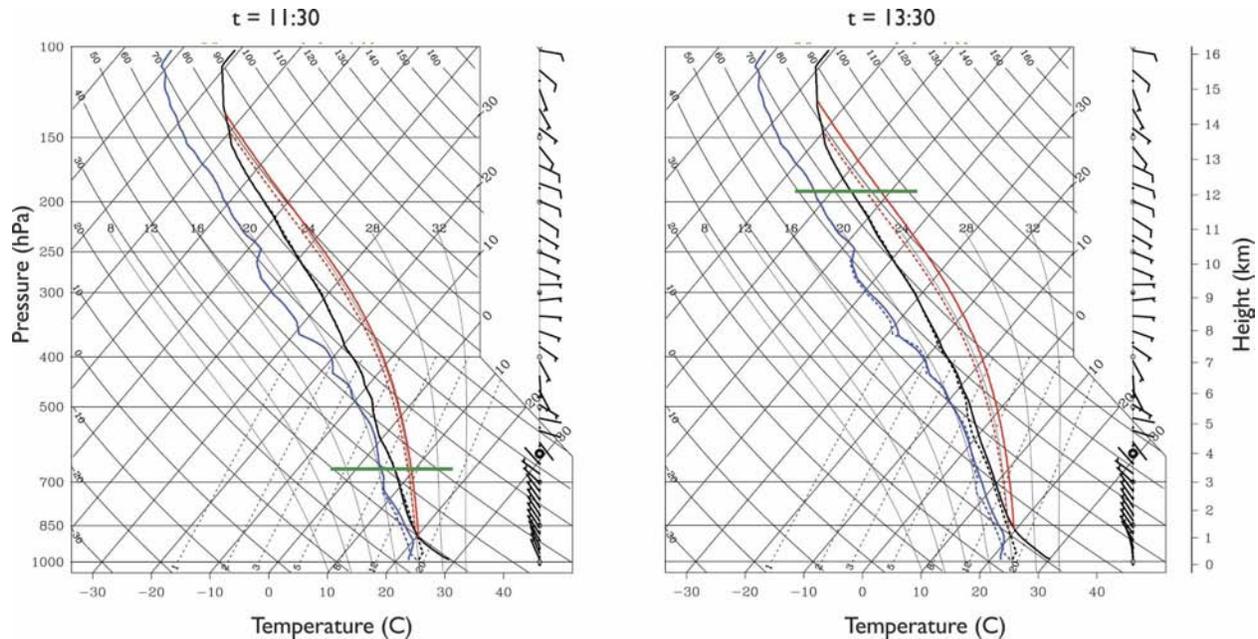
FIG. 4. The skew T–log$p$ diagram based on simulated mean profiles (left) before and (right) after transition to deep convection at 1130 and 1330 LT, respectively. Height of the cloud tops are shown by the horizontal green line. Initial morning sounding at 0730 LT is shown by the dashed line. Red lines show the pseudoadiabatic ascend trajectories from the level of free convection.

misrepresent the size of very elongated clouds. One may argue, however, that in the later case, the cloud size is itself a rather ambiguous concept. Note that this procedure counts the number of cloudy pixels that be-

long to clouds of various sizes but not the number of clouds; therefore, the integral of a PDF at a given level over all cloud sizes is the total cloud fraction at that level but is not the total number of clouds.
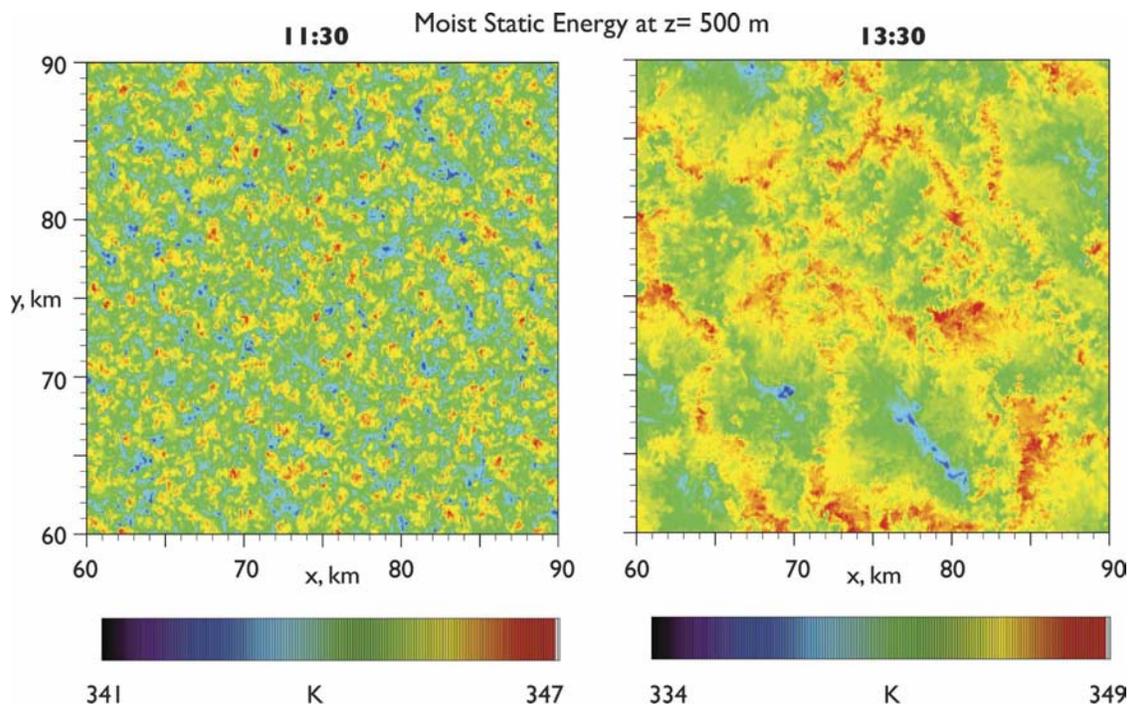

FIG. 5. Horizontal cross section through the moist static energy field at 500 m (left) before and (right) after transition to deep convection. Note that only about 1/5 of the actual domain width is shown.
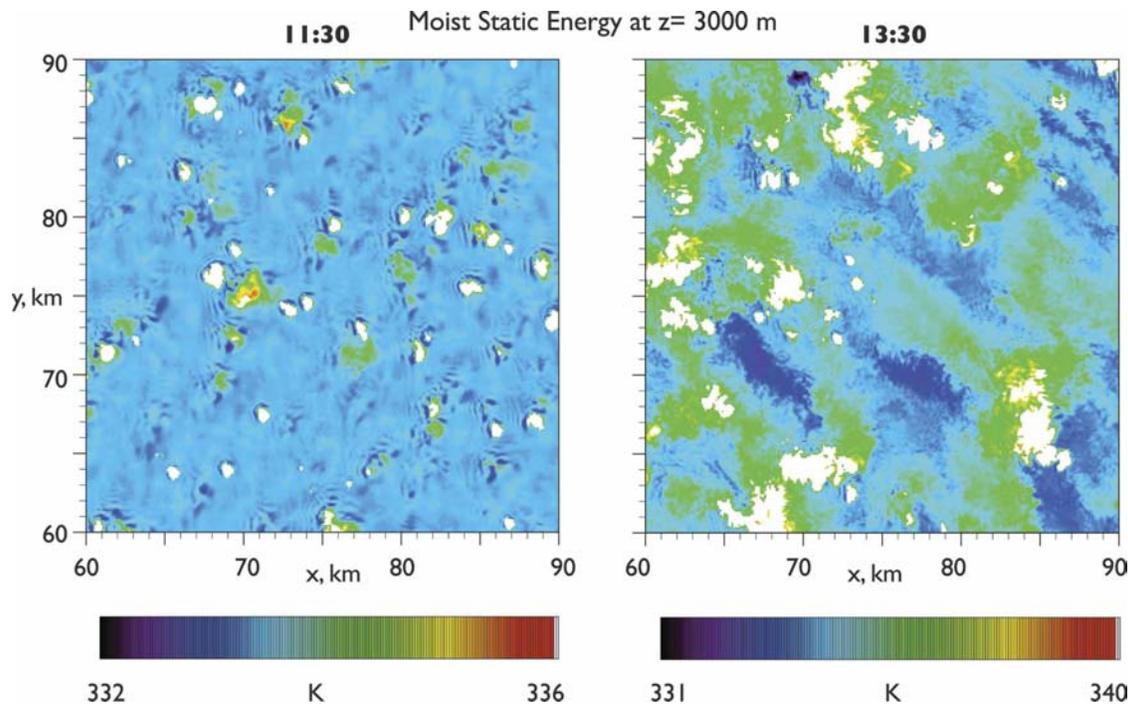
FIG. 6. As in Fig. 6 except for the 3000-m level. Clouds are masked by white color.

The cloud-size PDFs computed from the three-dimensional cloud-condensate fields at 1130, 1230, and 1330 LT are shown in Fig. 8. One can see that during the shallow convective regime (1130), the cloud population is rather narrow, with its mode at about 1 km, consistent with the eddy size in the simulated CBL at the same time, when no cold pools are present (see Fig. 6). During the congestus regime (1230) and especially deep cloud regime (1330), shallow and small clouds of the same size still produce the mode of the PDF; however, the PDFs near cloud base show the development of clouds as large as 4 km. Deep clouds at 1330 detrain into a layer between 8 and 12 km with anvils as large as 10 km. A few clouds shoot up as high as 15 km. Note that the cloud-size PDFs shown in Fig. 8 provide, by design, a measure of the relative contribution of clouds of various sizes to the total cloud fraction at a given height.

We can use the same cloud-size-measuring algorithm to stratify the in-cloud properties as a function of the cloud size; in other words, we can build a joint PDF of cloud size and some other in-cloud characteristic. Several examples of such joint PDFs are shown in Fig. 9. Each of the characteristics for each cloudy pixel was computed along the eight cloud-size measuring rays (see Fig. 7), then averaged for the cloud pixels that fall into the same cloud-size bin. First of all, one can see that above cloud base there is a clear tendency for the

in-cloud values of the maximum MSE (Fig. 9a) and total water content (Fig. 9b) to be larger for the bigger clouds. At the same time, near the cloud base, these characteristics are nearly identical for all clouds. These two features suggest that the bigger clouds are less diluted by entrainment, relative to smaller clouds. As a
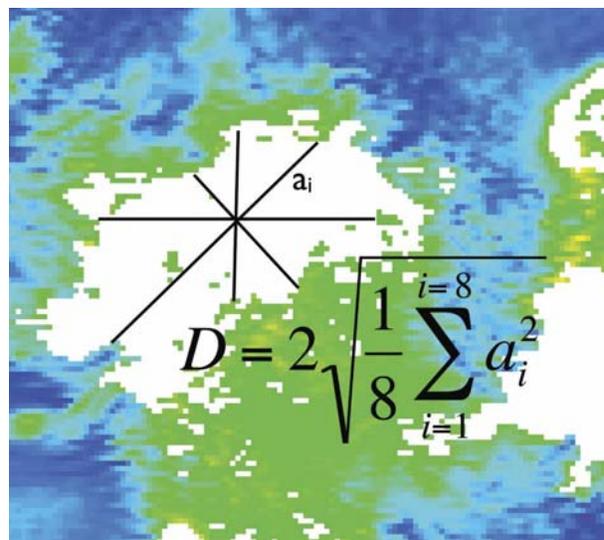

$$D = 2\sqrt{\frac{1}{8}\sum_{i=1}^{i=8} a_i^2}$$

FIG. 7. Schematic illustrating how the measurements of the cloud size were made for a given cloudy pixel (see the text for details).
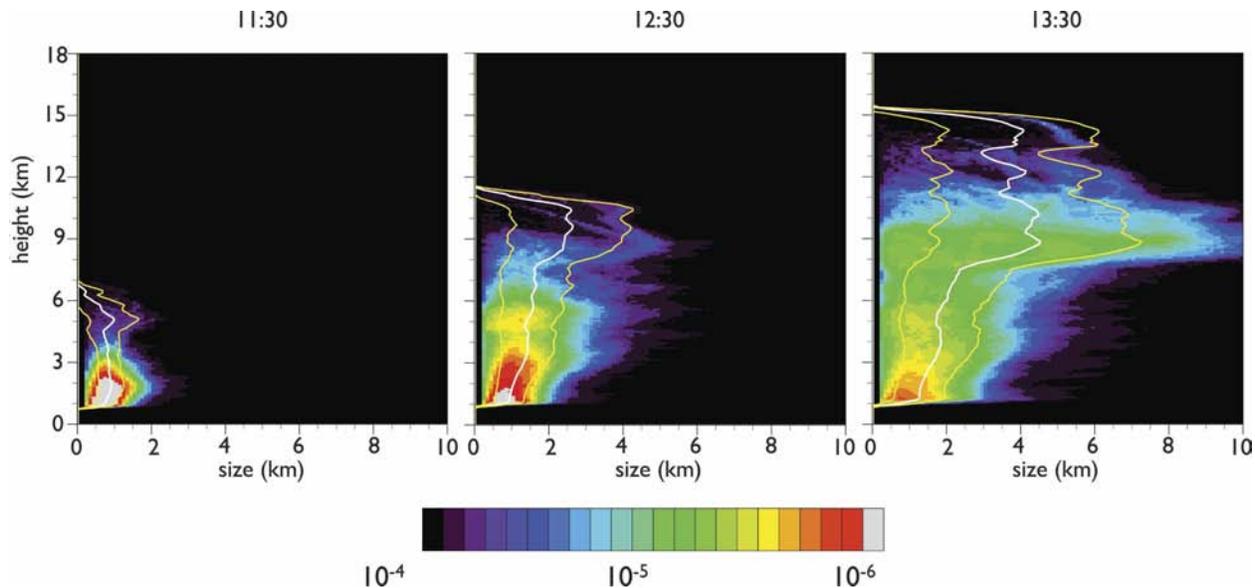
FIG. 8. PDF of cloud size as a function of height shown for three different simulation times. Mean and standard deviations are shown by the white and yellow lines, respectively.

result, the bigger clouds are able to penetrate higher. Because the bigger cloud are less diluted, they retain higher values of condensate, and, hence, are able to convert more water into precipitation, as illustrated in Fig. 9c. Less diluted clouds are more buoyant and, hence, maintain higher vertical velocities as shown in Fig. 9d. All of these results are compatible with the spectral cloud model introduced by Arakawa and Schubert (1974). The notion that bigger clouds can penetrate higher into the troposphere is also well illustrated by the PDF above 11 km, showing two very large clouds still ascending with considerable vertical velocities and which are wider than 4 km.

The result that bigger clouds maintain less diluted cores and climb higher as a result is well illustrated in Fig. 10, which shows the vertical cross section through a moist static energy field with a group of simulated clouds masked in white. Moist static energy is conserved under pseudoadiabatic processes and, thus, can be used as a tracer of the boundary layer air brought up by the clouds. One can see that the tallest cloud is also the widest one and has a mostly undiluted core. Note the highly turbulent nature of the simulated clouds and the spatial inhomogeneity of the boundary layer. It is also interesting to see streaks of higher values of the moist static energy in the middle troposphere, mostly from the contribution of the water vapor. These are the tracers of earlier clouds that have evaporated into the environment with subsequent further smearing by vertical shear of the mean horizontal wind.

c. PDF of moist static energy and entraining plumes

Because moist static energy is conserved for pseudoadiabatic processes and is unaffected by precipitation fallout, it has been often used to study mixing and entrainment processes in precipitating clouds. Strictly speaking, the MSE is conserved during the phase changes involving liquid water and water vapor and is not conserved for processes involving ice; however, the effect of ice on MSE conservation is relatively minor and, thus, for simplicity of qualitative analysis, is ignored in this study. The MSE is also a particularly useful quantity because the difference between a saturated parcel's MSE and the mean saturated MSE[3] at a given height is proportional to the parcel's thermal buoyancy (ignoring virtual temperature and loading effects). This provides a useful way of linking cloud thermodynamics and dynamics to study, for example, cloud mixing and entrainment processes.

Figure 11 shows the PDF of MSE as a function of height at 1130, 1230, and 1330 LT. The vertical profiles of the domain-averaged MSE and saturated MSE are represented by the green and red lines, respectively. One can see that rapid deepening of convection with time is accompanied by a broadening of the PDF, especially in the boundary layer. Most of the parcels have values of MSE close to the mean sounding. There is a

---

[3] Saturated moist static energy h_s is defined as $h_s = C_p T + gz + L q_s$, where q_s is saturation water vapor mixing ratio.
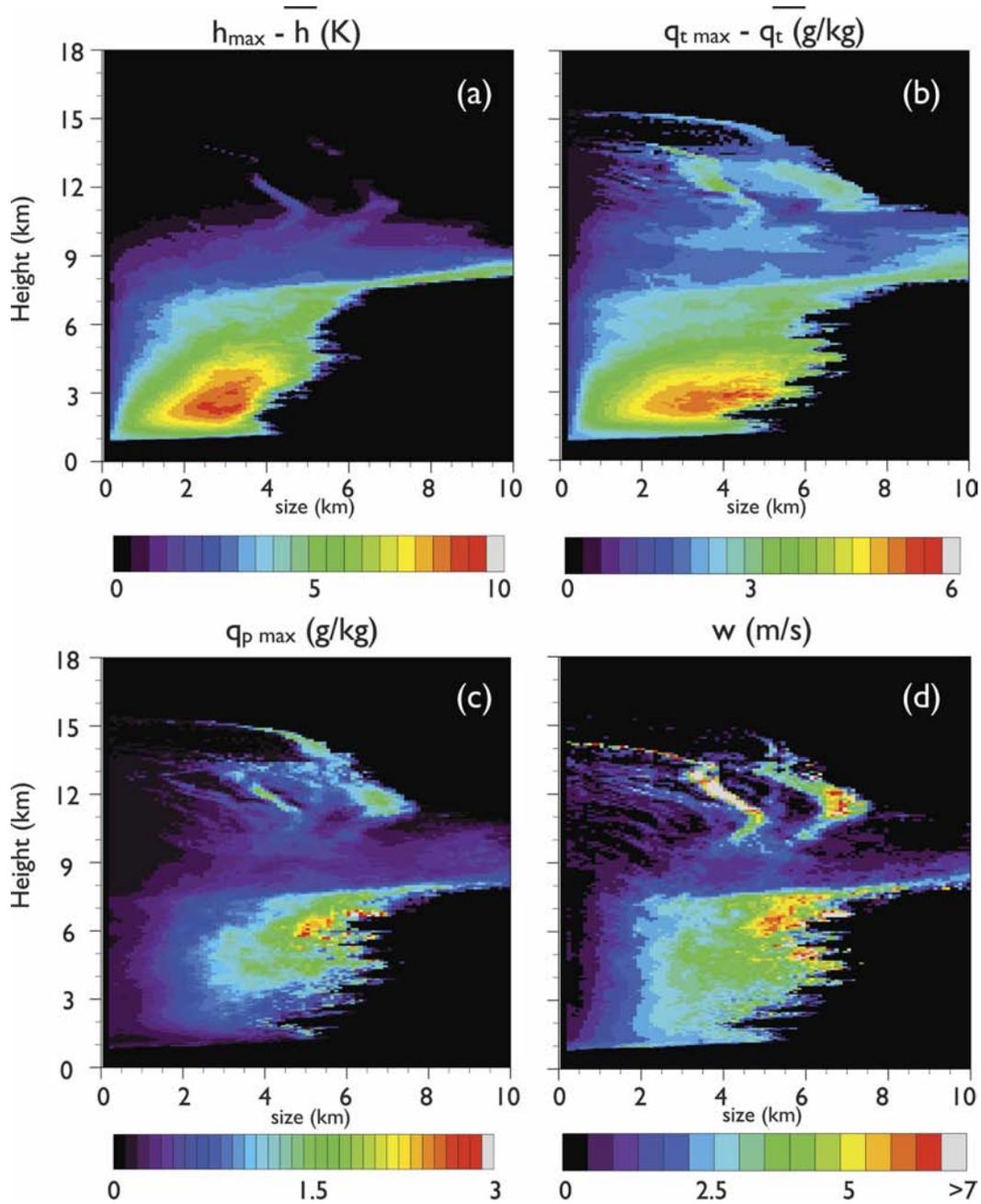
FIG. 9. Joint PDF of cloud size and several in-cloud characteristics: maximum deviation from the mean of (a) moist static energy and (b) total water content; (c) precipitating water content; and (d) mean vertical velocity. See text for details.

rather well-defined sharp boundary of minimum MSE at levels above 2 km. This boundary represents air with properties of the early morning sounding. In contrast, the right boundary of higher MSE is rather diffuse and, as shown further below, represents air in convective cores.

The white lines in Fig. 11 show the trajectories of parcels entraining according to a simple entraining-plume model commonly used in parameterizations of deep convection (e.g., Arakawa and Schubert 1974). According to that model, the vertical rate of change of in-plume moist static energy, h_c, is written as

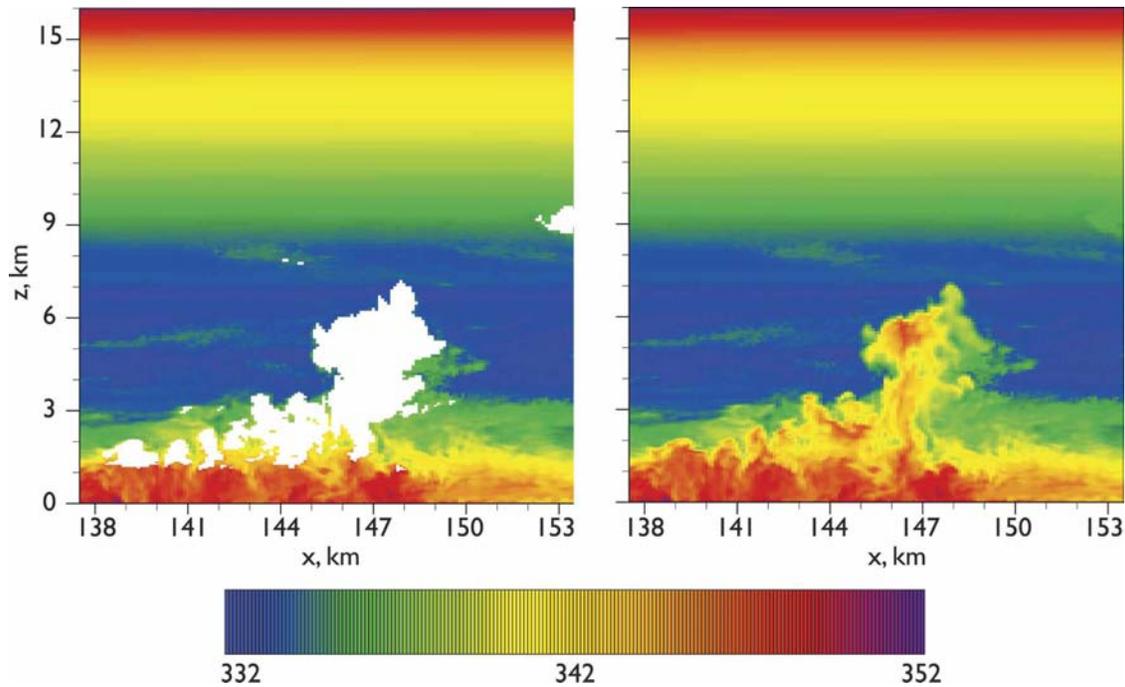$$\frac{\partial}{\partial z} \eta h_c = \lambda \eta \overline{h}, \tag{2}$$

FIG. 10. Vertical cross section through the moist static energy field. The left panel is identical to the right except for masking the position of clouds. Note that only about 1/10 of the actual domain width is shown.

where $\bar{h}$ is the mean profile, and η is the mass flux normalized by its value at cloud base, which obeys the continuity equation:

$$\frac{\partial}{\partial z}\eta = \lambda\eta, \qquad (3)$$

where λ is a nonnegative entrainment parameter. The white lines in Fig. 11 correspond to entraining plumes with different values of λ. The plume trajectories start at the same height and initially have the same value of moist static energy, chosen to approximate the corresponding quantities at the base of simulated clouds.
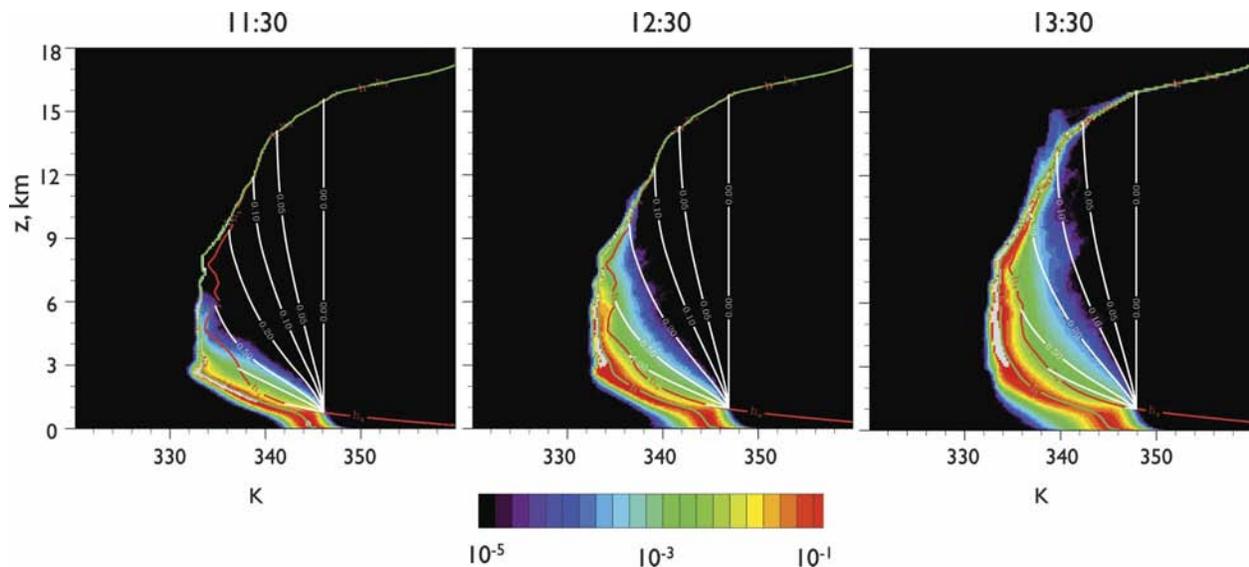

FIG. 11. PDF of moist static energy as a function of time for three different simulation times. White lines show the trajectories that the entraining plumes would follow given different values of entraining parameter, in km^{-1}: 0 (vertical line), 0.05, 0.1, 0.2, 0.5, 1.0. The mean moist static energy is shown by the green line; while saturated moist static energy is shown by the red line.
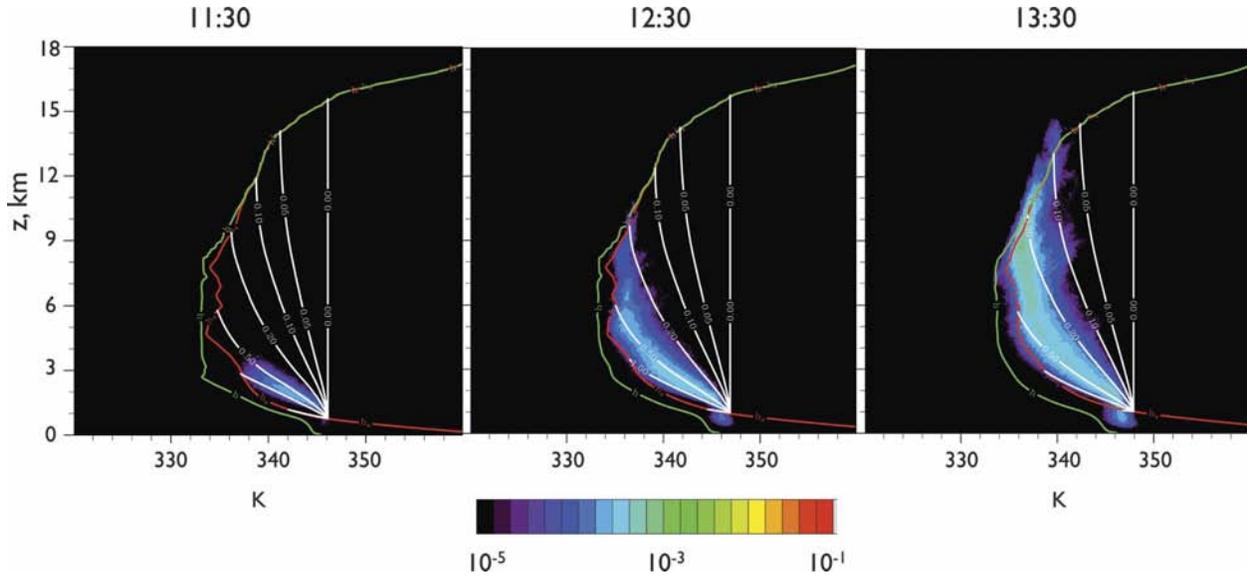
FIG. 12. As in Fig. 11 except for the updraft cores defined by the vertical velocity being in excess of 5 m s^{-1}.

The vertical white line corresponds to an undiluted parcel trajectory ($\lambda = 0$).

For a given height, the distance between the cloudy entraining-plume trajectory and the red line is proportional to the buoyancy of the entraining parcel. The maximum buoyancy may be achieved only by an undiluted ascending parcel; however, examination of Fig. 11 reveals no undiluted parcels rising from the subcloud layer to the level of neutral buoyancy. In fact, it appears that the least entraining cloud can be modeled rather well by the entraining plume with $\lambda = 0.1$ km^{-1}.

There is no direct analogy between the idealized entraining plumes and simulated clouds; however, we can substitute "plumes" with the convective cores, which we rather arbitrarily define as a collection of grid cells, cloudy or not, with vertical velocities exceeding 5 m s^{-1}. Figure 12 shows corresponding "core" PDFs normalized to be a subsample of the full PDFs shown in Fig. 11. Analysis shows that all cores above the boundary layer are cloudy. Also, the parcels in the dry cores in the boundary layer are, in fact, those that give rise to cloudy cores above. All the cores are positively buoyant except for the deepest ones in the upper troposphere where "overshooting" is apparent. Overall, the PDFs in Fig. 12 support the notion that the effect of entrainment on the clouds can be described rather well with a simple entraining-plume model (Lin and Arakawa 1997; KB05). Note that KB05 also used the superposition of PDFs and entraining-plume trajectories in their analysis.

Figure 13 shows the PDFs of MSE during the deep phase, conditionally sampled for the cloud-free environment and cloudy air. The latter is also subsampled into the cloudy updrafts ($w > 1$ m s^{-1}) and cloudy downdrafts ($w < -1$ m s^{-1}). One can see that the cloud-free air tends to closely pack around the mean profile between the mean saturated MSE profile and the early morning sounding profile. In the boundary layer, the range of MSE can be as large as 10 kJ kg^{-1}, as the air there is a mixture of parcels heated by the surface and those that have been brought down from the middle troposphere by convective downdrafts, as discussed above. The cloudy-air PDF is bounded by the mean MSE profile and maximum values in convective cores. One can also see that cloudy updrafts can be both positively and negatively buoyant, while cloudy downdrafts are predominantly negatively buoyant. It is interesting that all clouds seem to have a very narrow range of MSE at their bases; in fact, they "prefer" to have the highest MSE available at the boundary layer top, with the excess with respect to the mean sounding as high as 4 K.

4. Sensitivity experiments

The results of the high-resolution simulation, presented above, indicate that the rapid transition of convection from shallow to deep is strongly favored by a positive feedback involving evaporating precipitation; that is, larger clouds precipitate more heavily, which, through the cold pool dynamics, creates larger boundary layer thermals growing into even bigger clouds. The importance of such a precipitation feedback was tested by switching the evaporation of precipitation off and,
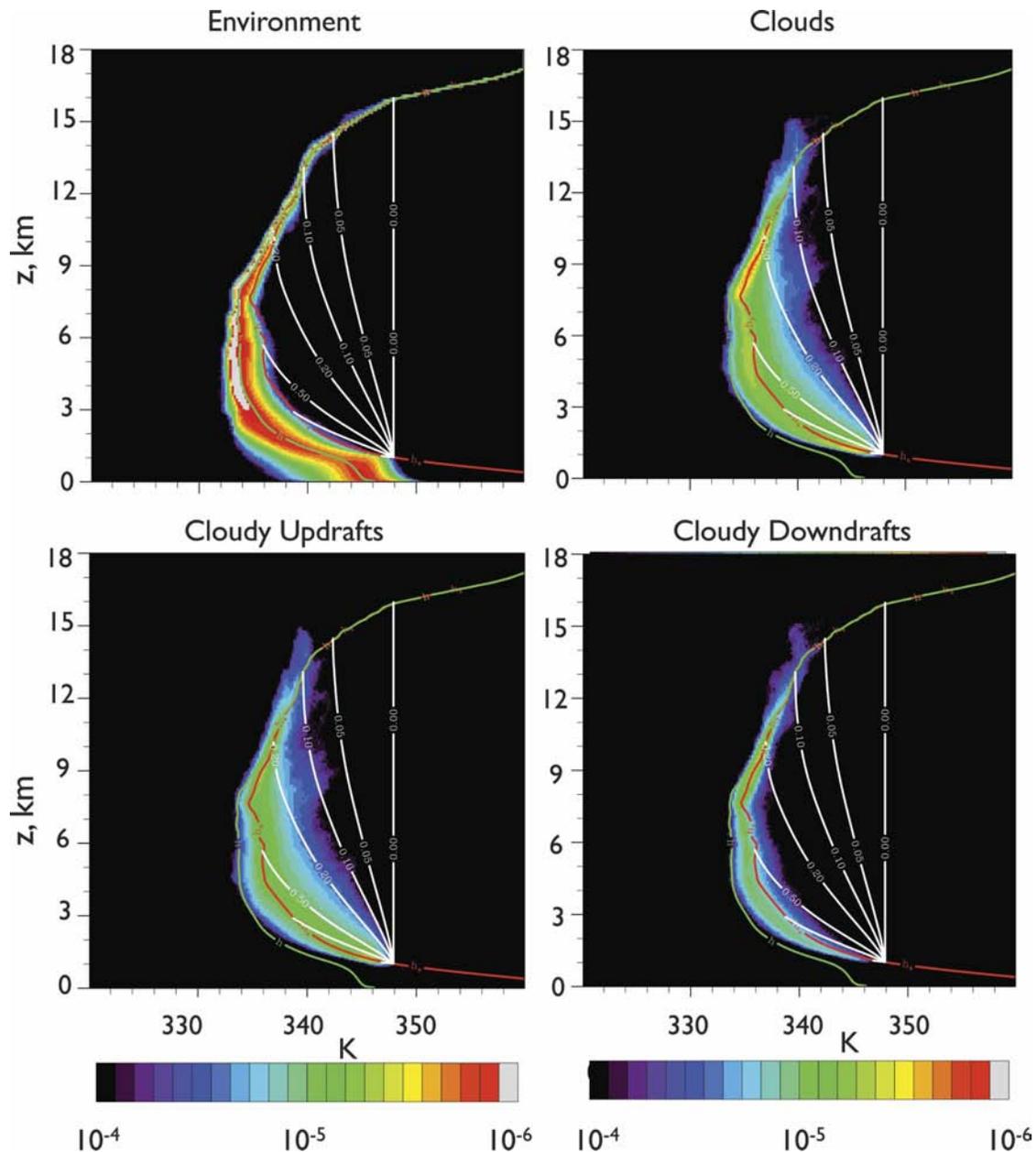
Fig. 13. Conditionally sampled PDF of moist static energy at the end of simulation: lines as in Fig. 11.

thus, preventing formation of large thermals via the colliding cold pool boundaries or gust fronts.

In addition to cold pool dynamics, there are other factors that can influence atmospheric convection. It is well established that the vertical growth of cumulus clouds can be influenced by the humidity in the free troposphere (e.g., Lin and Johnson 1996; Tompkins 2001a; Redelsperger et al. 2002). In this study, the troposphere is already quite moist (see the soundings in Fig. 4); therefore, additional moistening of the low troposphere during the relatively short shallow and con-

gestus cloud phase was not expected to have significant effect on the rate of cloud deepening. However, the effect of such additional moistening on cloud evolution was tested by replacing the initial water vapor profile above 1 km with the mean water vapor profile that developed by the end of the control simulation.

Wind shear also affects the development of convection and its organization (e.g., Rotunno et al. 1988; Wu and Yanai 1994; Robe and Emanuel 2001) and may even suppress convection (e.g., Xu et al. 1992). Soundings in Fig. 4 show a relatively modest amount of wind
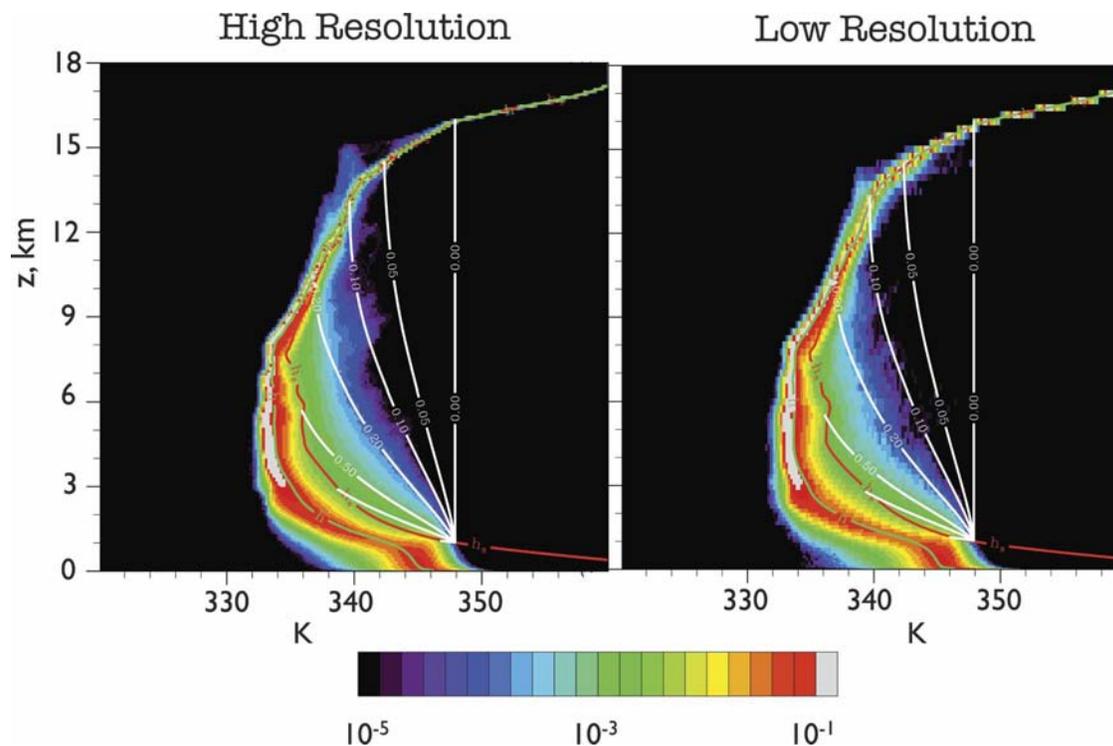
FIG. 14. PDF of moist static energy at the end of simulation for the high-resolution and lower-resolution runs: lines as in Fig. 11.

shear in the simulated environment. The effect of wind shear on the convection development as simulated in this study can be effectively eliminated by setting the prescribed horizontal wind at all levels to zero.

Since we have been limited by the amount of computational resources available, the sensitivity experiments have been conducted using lower spatial resolution. The horizontal grid spacing was increased from 100 to 250 m and the number of levels was cut in half, effectively doubling the vertical thickness of all the grid cells. The time step was also doubled. These measures allowed us to run the model in such a low-resolution configuration more than 30 times faster. The results of the control low-resolution simulation were compared with the results of its high-resolution counterpart and found to be quite similar. For example, Fig. 14 compares the PDFs of MSE at the end of simulations. One can see that PDFs are virtually identical, although there are some systematic differences. For example, the deep clouds in the low-resolution simulation tent to be deeper than in the high-resolution simulation. However, the general picture of the convection transition, and the boundary layer dynamics including the cold-pool dynamics, are quite similar.

The results of sensitivity experiments are shown in Fig. 15. As expected, additional moistening of the lower troposphere appears to have a minor effect on deepening of convection in this study because the free troposphere is already quite moist. However, even such a relatively modest prescribed increase in tropospheric moisture seems to increase the amount of both cloud condensate and precipitating water quite noticeably. The mean wind shear also appears to have quantitatively little effect on evolution of simulated clouds. Eliminating the cold-pool dynamics has by far the most dramatic effect on simulation. In fact, the convection remains predominantly shallow during the simulation, with some hint of congestus clouds but no deep clouds.

5. Summary and conclusions

In this paper, we present and discuss the results of a high-resolution three-dimensional simulation of shallow-to-deep convection transition over a relatively large area of about 150×150 km^2, using the forcing derived from an idealization of the observations made during the LBA experiment in Amazonia during the TRMM-LBA mission on 23 February 1999. The simulation starts from the early morning sounding at 0730 LT with a uniform initial state forced by prescribed surface latent and sensible heat fluxes that are applied uniformly. Horizontally uniform radiative cooling is
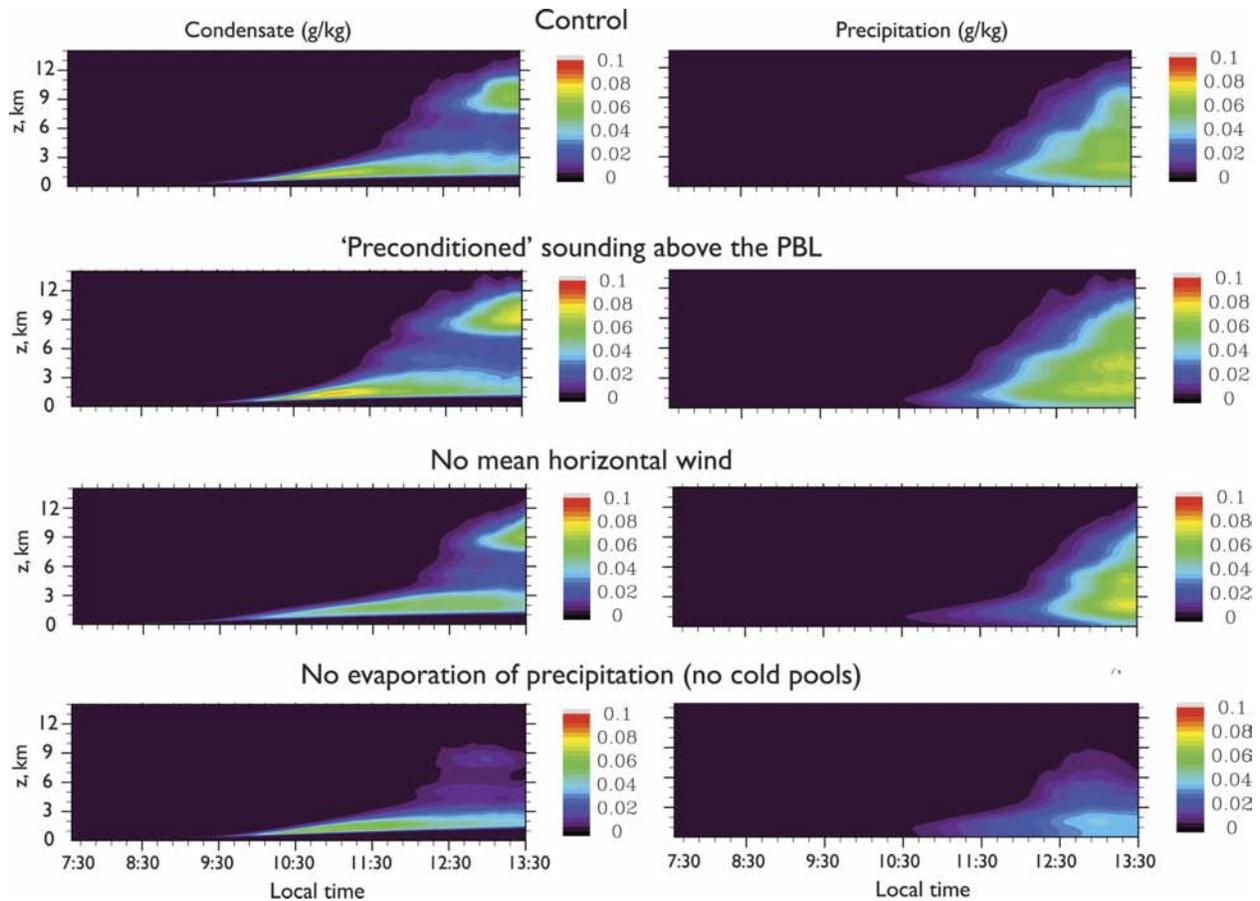
FIG. 15. Evolution of mean vertical profiles of (left) nonprecipitating cloud condensate and (right) precipitating water for the (top) control run and (bottom) three sensitivity runs (see text for details).

also prescribed. The simulation ends at 0130 in the afternoon.

Cumulus convection starts around 0930, first very shallow, stopping just above the boundary layer top, and later gradually developing into a layer of congestus clouds with tops just below the freezing level at about 5 km. Light precipitation starts first at about 1100 and increases quite dramatically shortly after the cloud tops breach the freezing level at about 1130, then keeps increasing until the end of the simulation. Throughout the simulation, including the initial state, the mean thermodynamic sounding has a rather considerable amount of CAPE, in the range from about 1600 J kg^{-1} in the early morning to 2400 J kg^{-1} at the end of the simulation, with virtually no CIN. Theoretically, clouds could rise as high as 12 km as early as at 0930; however, deep clouds emerge only at about 1230 in the afternoon. This is because the clouds during the shallow and congestus stages have sizes (i.e., horizontal scales) comparable to the sizes of boundary layer eddies, that is, generally less than 1 km, and are fairly quickly diluted

by the environmental air through entrainment. This prevents deep clouds from forming. Thus the existence of positive buoyancy through a deep layer is not by itself sufficient to permit deep convection, even in an environment characterized by low convective inhibition; however, such triggering is often allowed in cumulus parameterizations.

The rapid evolution of the cloud population during the transition has been studied by comparing the cloud size PDF during the shallow, congestus and deep convection phases. It is shown that during all of these phases, the shallow clouds dominate the mode of the PDFs at about 1-km size. During the deep phase, the PDFs show cloud bases as wide as 4 km with anvils as large as 10 km. The joint PDFs of cloud size and other in-cloud variables such as total water, moist static energy, and vertical velocity show that the bigger clouds are far less diluted above their bases than their smaller counterparts. As a result, the bigger clouds are more buoyant and, therefore, maintain high in-core vertical velocities, and penetrate deeper into the troposphere.

It is demonstrated that the transition of convection from shallow to deep is strongly favored by a positive feedback involving evaporating precipitation. Larger clouds precipitate more heavily and, thus, through the cold pool dynamics, tend to produce larger boundary layer thermals that may grow into even larger precipitating clouds. This feedback, first discussed by KB05, is eliminated in a sensitivity experiment by artificially switching off the evaporation of precipitation. As a result, big thermals are not created and the convection remains shallow during the whole simulation period, with a few congestus but no deep clouds.

The effect of additional moistening of the troposphere during the shallow and congestus phases on subsequent development of deep convection is also tested and found to be relatively minor. This is because, in the case studied here, the lower and middle troposphere are already quite moist (see Fig. 4). Had those levels been significantly drier, the effects of tropospheric moisture on vertical development of convection could dominate. Wind shear was also of secondary importance for the transition to deep convection, for the case studied here.

During the deep convective phase, the range of moist static energy in the boundary layer is about 10 kJ kg^{-1}. The distribution is skewed toward the lower values due to convective downdrafts. The clouds seem to grow from the parcels that have the highest values of moist static energy in the boundary layer, which in our simulation exceed the mean value by as much as 4 K. It is remarkable that regardless of cloud size, the thermodynamic properties at cloud bases are nearly identical for all of the simulated clouds, in agreement with the findings of KB05.

Examination of the PDFs of moist static energy as a function of height reveals no undiluted parcels rising from the subcloud layer to the level of neutral buoyancy. The PDFs of convective cores, defined as grid cells with vertical velocities exceeding 5 m s^{-1} and used as proxies for the entraining plumes used in some convective parameterizations (e.g., Arakawa and Schubert 1974), generally support earlier findings (Lin and Arakawa 1997; KB05) that the effect of entrainment on clouds can be described rather well with such a simple model. It appears that that the least diluted plume in the simulation corresponds to a fractional entrainment rate of about 0.1 km^{-1}.

In this paper, we have deliberately avoided the subject of the sensitivity of the results to grid resolution, domain geometry, and size, apart from the sensitivity experiments discussed in this paper that used the doubled grid spacing. Some discussion of such issues for this particular case in the scope of CRM intercomparison can be found in the paper by Grabowski et al. (2005). It is quite possible that even resolution as fine as 100 m is still too coarse to properly resolve the entrainment by simulated clouds. The current state of computational technology and resources available to us at the time of this study have precluded us from comprehensive tests of the effects of higher grid resolution. We feel, however, that the subject of grid sensitivities of simulated diurnal cycle of convection over land is important enough to warrant a future study especially in the context of recent advances in the area of cloud-resolving global climate modeling.

REFERENCES

Arakawa, A., 2004: The cumulus parameterization problem: Past, present, and future. *J. Climate,* **17,** 2493–2525.

——, and W. H. Schubert, 1974: Interaction of a cumulus cloud ensemble with the large-scale environment, Part I. *J. Atmos. Sci.,* **31,** 674–701.

Avissar, R., 1995: Scaling of land–atmosphere interactions: An atmospheric modeling prospective. *Hydrol. Processes,* **9,** 679–695.

Bechtold, P., J.-P. Chaboureau, A. Beljaars, A. K. Betts, M. Kohler, M. Miller, and J.-L. Redelsperger, 2004: The simulation of the diurnal cycle of convective precipitation over land in global models. *Quart. J. Roy. Meteor. Soc.,* **130,** 3119–3137.

Betts, A. K., and C. Jakob, 2002: Evaluation of the diurnal cycle of precipitation, surface thermodynamics, and surface fluxes in the ECMWF model using LBA data. *J. Geophys. Res.,* **107,** 8045, doi:10.1029/2001JD000427.

Bluestein, H. B., and S. S. Parker, 1993: Modes of isolated, severe convective storm formation along the dryline. *Mon. Wea. Rev.,* **121,** 1354–1372.

Grabowski, W. W., 2001: Coupling cloud processes with the large-scale dynamics using the Cloud-Resolving Convection Parameterization (CRCP). *J. Atmos. Sci.,* **58,** 978–997.

——, and Coauthors, 2006: Daytime convective development over land: A model intercomparison based on LBA observations. *Quart. J. Roy. Meteor. Soc.,* **132,** 317–344.

Khairoutdinov, M. F., and D. A. Randall, 2001: A cloud resolving model as a cloud parameterization in the NCAR Community Climate System Model: Preliminary results. *Geophys. Res. Lett.,* **28,** 3617–3620.

——, and ——, 2003: Cloud resolving modeling of the ARM summer 1997 IOP: Model formulation, results, uncertainties and sensitivities. *J. Atmos. Sci.,* **60,** 607–625.

——, ——, and C. DeMotte, 2005: Simulations of the atmospheric general circulation using a cloud-resolving model as a super-parameterization of physical processes. *J. Atmos. Sci.,* **62,** 2136–2154.

Kingsmill, D. E., 1995: Convection initiation associated with a sea-breeze front, a gust front, and their collision. *Mon. Wea. Rev.,* **123,** 2913–2933.

Kuang, Z., and C. S. Bretherton, 2005: A mass-flux scheme view of a high-resolution simulation of transition from shallow to deep cumulus convection. *J. Atmos. Sci.,* **63,** 1895–1909.

Lin, C., and A. Arakawa, 1997: The macroscopic entrainment processes of simulated cumulus ensemble. Part II: Testing the entraining-plume model. *J. Atmos. Sci.,* **54,** 1044–1053.

Lin, X., and R. Johnson, 1996: Heating, moistening, and rainfall over the western Pacific warm pool during TOGA COARE. *J. Atmos. Sci.,* **53,** 3367–3383.

Randall, D. A., M. Khairoutdinov, A. Arakawa, and W. Grabowski, 2003a: Breaking the cloud-parameterization deadlock. *Bull. Amer. Meteor. Soc.,* **84,** 1547–1564.

——, and Coauthors, 2003b: Confronting models with data: The GEWEX Cloud Systems Study. *Bull. Amer. Meteor. Soc.,* **84,** 455–469.

Redelsperger, J.-L., and T. L. Clark, 1990: The initiation and horizontal scale selection of convection over gently sloping terrain. *J. Atmos. Sci.,* **47,** 516–541.

——, D. B. Parsons, and F. Guichard, 2002: Recovery processes and factors limiting cloud-top height following the arrival of a dry intrusion observed during TOGA-COARE. *J. Atmos. Sci.,* **59,** 2438–2457.

Robe, F. R., and K. A. Emanuel, 2001: The effect of vertical wind shear on radiative–convective equilibrium states. *J. Atmos. Sci.,* **58,** 1427–1445.

Rotunno, R., J. B. Klemp, and M. L. Weisman, 1988: A theory for long-lived squall lines. *J. Atmos. Sci.,* **45,** 463–485.

Siebesma, A. P., and Coauthors, 2003: A large-eddy simulation intercomparison study of shallow cumulus convection. *J. Atmos. Sci.,* **60,** 1201–1219.

Silva Dias, M. A. F., and Coauthors, 2002: Clouds and rain processes in a biosphere atmosphere interaction context in the Amazon Region. *J. Geophys. Res.,* **107,** 8072, doi:10.1029/2001JD000335.

Tompkins, A. M., 2001a: Organization of tropical convection in low vertical wind shears: The role of water vapor. *J. Atmos. Sci.,* **58,** 529–545.

——, 2001b: Organization of tropical convection in low vertical wind shears: The role of cold pools. *J. Atmos. Sci.,* **58,** 1650–1672.

Wakimoto, R. M., 1982: The life cycle of thunderstorm gust fronts as viewed with Doppler radar and rawinsonde data. *Mon. Wea. Rev.,* **110,** 1060–1082.

——, and N. T. Atkins, 1994: Observations of the sea breeze front during CaPE. Part I: Single-Doppler, satellite, and cloud photogrammetry analysis. *Mon. Wea. Rev.,* **122,** 1092–1114.

Weckwerth, T. M., J. W. Wilson, and R. M. Wakimoto, 1996: Thermodynamic variability within the convective boundary layer due to horizontal convective rolls. *Mon. Wea. Rev.,* **124,** 769–784.

Wu, X., and M. Yanai, 1994: Effects of vertical wind shear on the cumulus transport of momentum: Observations and parameterization. *J. Atmos. Sci.,* **51,** 1640–1660.

Xu, K.-M., A. Arakawa, and S. K. Krueger, 1992: The macroscopic behavior of cumulus ensembles simulated by a cumulus ensemble model. *J. Atmos. Sci.,* **49,** 2421–2436.